Heliyon 10 (2024) e38209

Contents lists available at ScienceDirect

Heliyon

journal homepage: www.cell.com/heliyon

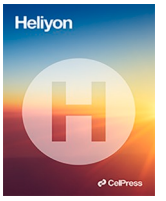

Research article

Design and study of additively manufactured Three periodic minimal surface (TPMS) structured porous titanium interbody cage

Kun Li [a], ChunYan Tian [a], QiuJiang Wei [a], XinRui Gou [a], FuHuan Chu [a], MengJie Xu [a], LinHui Qiang [a,b,c,**], ShiQi Xu [a,b,c,*]

[a] Department of Biomedical Engineering, Chengde Medical University, HeBei Province, China
[b] Hebei International Joint Research Center for Biomedical Engineering, Chengde Medical University, Hebei Province, China
[c] Chengde Medical Additive Manufacturing Technology Innovation Center, Chengde Medical University, Hebei Province, China

ARTICLE INFO

Keywords:
Three periodic minimal surfaces
Cervical interbody cage
3D printing
Tubular-G

ABSTRACT

Objective: TPMS porous structures have adjustable stiffness, a smooth surface, and highly connected pores, which help avoid stress concentration within the dot-matrix structure and promote cell adhesion and proliferation. A cervical interbody cage based on this type of porous structure was designed and fabricated, and its mechanical properties and biocompatibility were evaluated.
Methods: TPMS porous structures have adjustable stiffness, a smooth surface, and highly connected pores, which help avoid stress concentration within the dot-matrix structure and promote cell adhesion and proliferation. A cervical interbody cage based on this type of porous structure was designed and fabricated, and its mechanical properties and biocompatibility were evaluated.
Results: The volume fraction of the 3D-printed TC4-based Tubular-G structure was linearly related to compressive strength. Adjusting the volume fraction resulted in a Tubular-G structure with a modulus and yield strength similar to human bone, without stress concentration within the structure. The designed and fabricated TC4-based Tubular-G porous cervical interbody cage demonstrated excellent anti-sagging properties and biocompatibility.
Conclusions: The volume fraction of the 3D-printed TC4-based Tubular-G structure was linearly related to compressive strength. Adjusting the volume fraction resulted in a Tubular-G structure with a modulus and yield strength similar to human bone, without stress concentration within the structure. The designed and fabricated TC4-based Tubular-G porous cervical interbody cage demonstrated excellent anti-sagging properties and biocompatibility.

1. Introduction

Cervical interbody cages are medical devices used to treat damaged intervertebral discs in the cervical region, which are used to permanently fix adjacent vertebrae at the lesion site, reduce the pressure on the nerve root or spinal cord caused by instability of the vertebrae at the lesion site, and alleviate the patient's pain [1–4]. The cervical cages currently used in clinical practice are mainly

* Corresponding author. Department of Biomedical Engineering, Chengde Medical University, Chengde, Hebei, 067000, China.
** Corresponding author. Department of Biomedical Engineering, Chengde Medical University, HeBei Province, China
E-mail address: xushiqi@cdmc.edu.cn (S. Xu).

https://doi.org/10.1016/j.heliyon.2024.e38209
Received 28 June 2024; Received in revised form 2 September 2024; Accepted 19 September 2024
Available online 20 September 2024

prepared from polyether ether ketone (PEEK) or titanium alloy, which have good biocompatibility and chemical stability. The PEEK material has been more widely used because it has a similar modulus of elasticity to human bone and is easy to produce using conventional machining methods. In order to solve the problem of poor imaging effect of PEEK material in CT and other imaging examinations, commercial PEEK cervical interbody cages need to introduce titanium or tantalum wire to enhance its imaging effect in imaging examinations.

Titanium alloys are widely used to manufacture bone implants, such as bone splints, bone nails, and titanium mesh for cranial bone repair, due to their superior biocompatibility and corrosion resistance [5,6]. However, the elastic modulus of titanium alloys (110–120 GPa) is significantly higher than that of human bone (0.02–23.8 GPa) [7]. A homogeneous cervical interbody cage made by direct machining can have an elastic modulus of up to 110 GPa, which may lead to "stress shielding" after implantation. This stress shielding effect can result in subsidence and displacement of the cage post-surgery [8]. Introducing a porous structure into the titanium cervical cage can significantly lower its elastic modulus, making it more compatible with human cervical vertebrae and reducing the risk of stress shielding. However, directly machining these porous structures in titanium alloy cervical interbody cages poses significant challenges [9].

With the advancement of metal additive manufacturing technology, it has become possible to construct complex porous structures in titanium alloys using 3D printing. Selective Laser Melting (SLM) technology has been widely reported for fabricating titanium alloy-based porous structures for orthopedic implant applications. Christian Yee-Yanagishita et al. [10] used titanium alloy 3D printing to fabricate porous titanium alloy intervertebral cages, titanium alloy truss intervertebral cages, and PEEK porous cages for mechanical and dynamic subsidence testing. Their results showed that the titanium porous interbody cage exhibited the best subsidence performance among the three types. Marie Cronskär et al. [9] utilized titanium 3D printing to produce a customized hip stem, demonstrating that 3D printing effectively reduces fatigue limits and manufacturing costs compared to conventional machining methods. Chia-Hsuan Li et al. [11] used 3D printing to fabricate a mandibular implant for cosmetic reconstruction and restoration in patients with severe mandibular defects. Studies have verified that 3D-printed porous titanium alloy bone implants exhibit mechanical properties that better match human bone, but they also highlight the limitations of conventional dot-matrix porous structures, which are prone to stress concentration [12]. The susceptibility of dot-matrix structures to stress concentrations stems from their structural peculiarities. These structures typically feature numerous connection points that are geometrically complex and prone to abrupt shape changes or discontinuities. Such features can lead to stress concentrations, which negatively impact the material's fatigue life.

Triple periodic minimal surface (TPMS) is a smooth, periodic implicit surface with zero mean curvature. It enables precise tuning of morphological parameters such as pore size, porosity, and structure thickness. The continuous, smooth surfaces of TPMS structures offer better mechanical properties compared to point structures, as they avoid the stress concentrations commonly found in point structures [12]. Studies on the mechanical properties of TPMS structures have demonstrated their suitability for fabricating bone implants [13–16]. Nejc Novak et al. [17]demonstrated that TPMS structures exhibit excellent energy absorption capabilities and show significant potential for crashworthiness applications. Beyond basic TPMS structures, some researchers have optimized these structures and proposed novel and advanced solutions with considerable development potential. For instance, Miao Zhao et al. [18] introduced a new interpenetrating lattice structure based on the TPMS framework, which reduces structural compliance by more than 10.85 % compared to conventional TPMS structures, highlighting its potential for lightweight applications.

In the study of TPMS structures applied to artificial lumbar spine implants, Peng Shang et al. [19] used 3D printing to fabricate an artificial lumbar spine cone implant with a TPMS structure. The results showed that the TPMS-based implant had higher compressive strength and a lower tendency to subside compared to conventional designs. This study highlights the great potential of TPMS structures for interbody cage design. However, the research focused on a single configuration of an artificial spine cone and did not fully explore other potential applications of TPMS structures in implants.

The Gyroid, an infinitely connected TPMS, was discovered by Alan Schoen in 1970 [20]. Many Gyroid structures exist in nature, such as in butterfly wings and bird feathers [21,22]. Compared to other types of TPMS, the Gyroid exhibits superior manufacturability, mechanical properties, and enhanced cell adhesion and proliferation characteristics [14]. Xiaoyu Du et al. [23] investigated 3D-printed Gyroid structures made from polyether ether ketone/silicon and found that these structures offer advantages like a large surface area and uniform stress distribution under load. Additionally, gradient Gyroid structures have shown potential in lightweight and energy absorption applications. For instance, Miao Zhao et al. [24] designed functionally graded sheet structures for Primitive and Gyroid configurations, increasing energy absorption by 60 % and highlighting a broader application potential for Gyroid structures. The Tubular-G structure, a variation of the Gyroid, has a continuous smooth curved surface similar to bone trabeculae, suggesting that its application in bone implants could yield improved results.

Based on this, we propose to characterize the compressive strength and stress distribution of Tubular-G structural units using the SLM metal 3D printing technique combined with finite element analysis. The Tubular-G structure was further applied to the design of cervical interbody cages. By adjusting the parameters of the Tubular-G structure, various cervical interbody cage models with different properties were constructed. The cervical interbody cage structure was optimized by establishing the relationship between the Tubular-G structure parameters and the apparent elastic modulus of the cage. Additionally, the stiffness, simulated subsidence, and biocompatibility of different cervical interbody cages were evaluated to identify a model that combines superior mechanical properties with enhanced biocompatibility.

2. Materials and methods

2.1. Design of the Tubular-G unit

The Tubular-G structure, as a deformation of the Gyriod structure, has the following implicit surface equations [25]:

$$10*(cos(2*\pi*x)*cos(2*\pi*y)+cos(2*\pi*y)*cos(2*\pi*z)+cos(2*\pi*z)*cos(2*\pi*x))-0.5*(cos(4*\pi*x)*cos(4*\pi*y)+cos(4*\pi*y)*cos(4*\pi*z)+cos(4*\pi*z)*cos(4*\pi*x))-14=C \quad (1)$$

where C is the offset parameter, which shows a linear relationship with the volume fraction of the Tubular-G structure after fitting, as shown in Fig. 1. This parameter can be adjusted to precisely control the volume fraction of the Tubular-G structure, thereby synchronizing the pore size.

Due to the limitations of SLM printing accuracy for titanium alloys, the cell size was set to 2 mm. The pore sizes corresponding to 10 %, 20 %, 30 %, 50 %, and 70 % volume fractions at this cell size are shown in Table 1. According to the literature, bone tissue regeneration requires a minimum pore size of 100 μm, and pore sizes larger than 300 μm are favorable for cell proliferation [26]. Hollister et al. suggested that pore sizes between 300 and 1200 μm do not significantly differ in osteogenesis [27]. The pore size for the 10 % volume fraction was deemed too large, so we selected 20 %, 30 %, 50 %, and 70 % volume fractions for our study. For instance, the pore size for the 50 % volume fraction structure was measured as shown in Fig. 2.

Relevant studies have shown that with increasing the number of porous structures' single-cell arrays, the corresponding structure's equivalent elastic modulus will gradually converge to a limiting value. When the number of single cells reaches 4*4*4, the equivalent elastic modulus of the corresponding structure is approximately equal to that of the macroscopic model of bone scaffolds [28]. We arrayed the models with four-volume fractions as cubes according to 4*4*4 to study the mechanical properties of the Tubular-G structure, as shown in Fig. 3.

2.2. SLM printing

This study used a direct metal laser sintering machine (EOS EOSINT M 280, EOS Gmbh, Germany) to fabricate Tubular-G structural samples. The printer used a 100 μm laser beam spot, a 100 °C preheating temperature, and a 50 μm powder thickness. The Ti6Al4V powder conformed to ISO 5832–3 with an average particle size of 50 μm.

After 3D printing, the samples were immersed in distilled water in an ultrasonic cleaner for half an hour to remove unsintered powder. Three copies of each sample were printed for each volume fraction (Fig. 4).

2.3. Mechanical properties testing

Axial compression tests were conducted on the Ti6Al4V fabricated Tubular-G structure samples in Section 2.3 to obtain their equivalent elastic modulus, yield strength, and peak load. The tests were performed using a universal testing machine (MTS-E44.305, USA). The samples were secured in a compression fixture and compressed axially at a rate of 0.5 mm/min. The loads and displacements during compression were recorded until the samples fractured. To ensure experimental reproducibility, three tests were conducted for each of the four volume fractions of the Tubular-G structures (20 %, 30 %, 50 %, and 70 %), totaling 12 experiments.

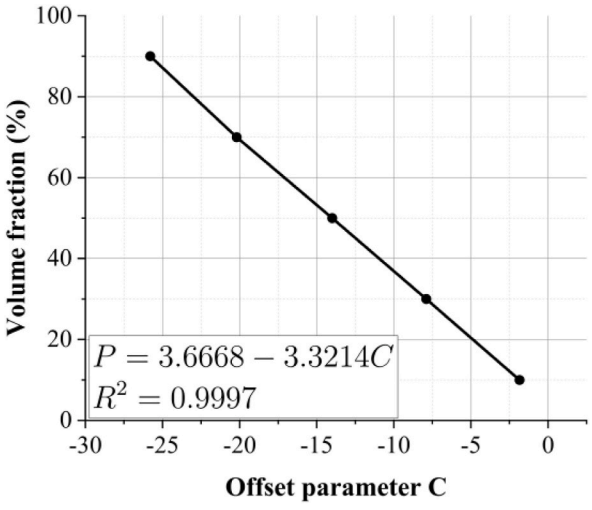

Fig. 1. Offset parameter versus volumetric fraction.

Table 1
The pore size of 2 mm Tubular-G units at different volume fractions.

volume fraction	10 %	20 %	30 %	50 %	70 %
pore size (μm)	1620	1450	1200	1000	720

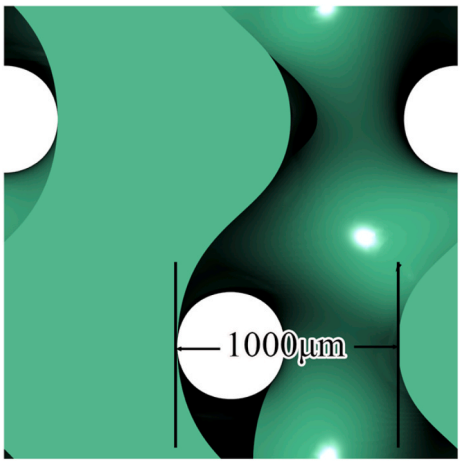

Fig. 2. Measurement of the pore size.

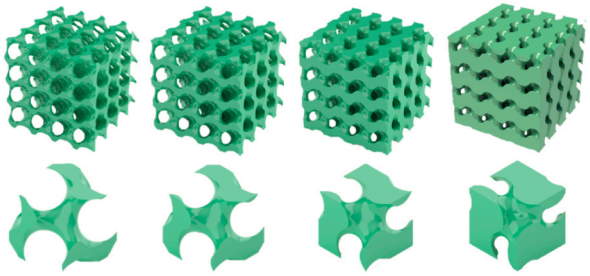

Fig. 3. 20 %, 30 %, 50 %, and 70 % volume fractions after 4*4*4 array Tubular-G.

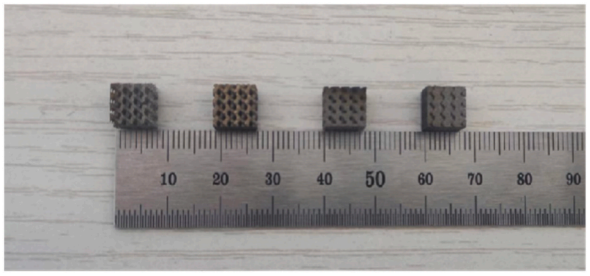

Fig. 4. 3D printed Tubular-G structures in four volume rates, from left to right, 20 % volume fraction, 30 % volume fraction, 50 % volume fraction, and 70 % volume fraction.

2.4. Finite element simulation

Finite element analysis was used to observe the internal stress distribution of the Tubular-G structure when compressed to its yield strength, identifying any potential stress concentration issues. To compare with the dot-matrix structure, a finite element model of the body-centered cubic structure was also established. Stress nephograms of both structures under the same load were obtained to highlight their differences in stress distribution. The body-centered cubic structure is shown in Fig. 5.

To determine the appropriate mesh size for the FEA, a convergence analysis was performed using a Tubular-G structure with a 20 %

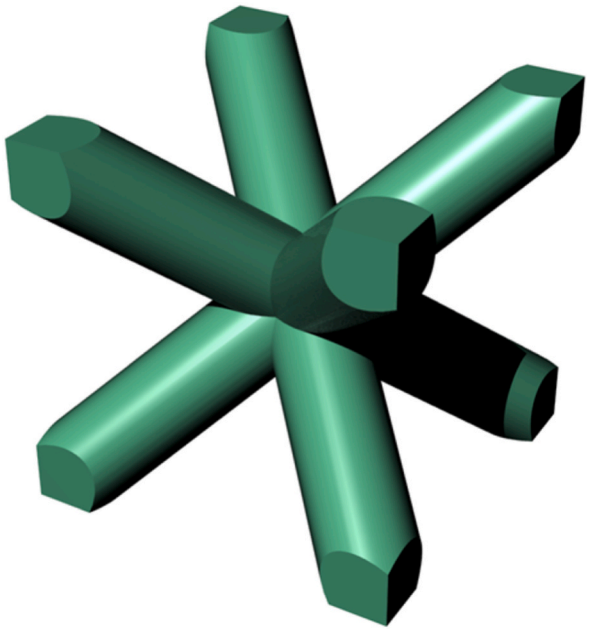

Fig. 5. The body-centered cubic structure.

volumetric fraction. After fully considering the accuracy and efficiency of the simulated compression process, the mesh size was chosen to be 0.11 mm. The finite element models of the Tubular-G structure and body-centered cubic structure were constructed using Abaqus 2022a (Dassault Systèmes), featuring 4 × 4 × 4 arrays with four volume fractions, and meshed with 0.11 mm C3D10M elements. The

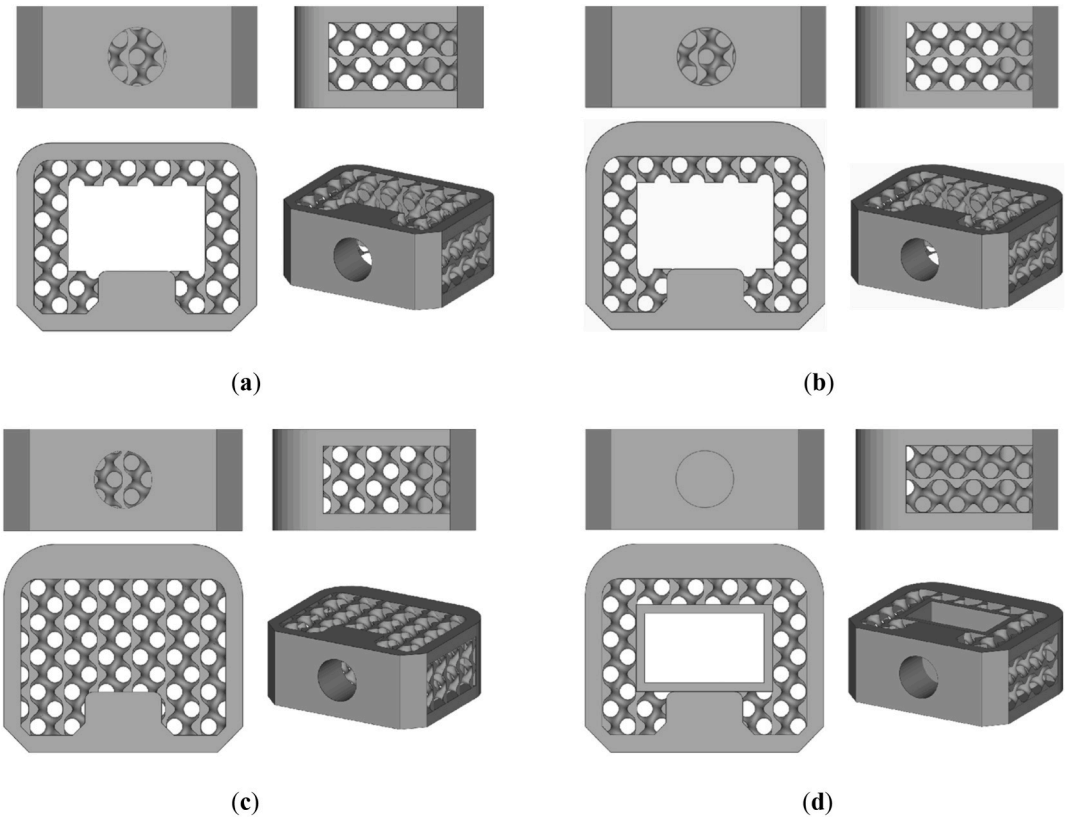

Fig. 6. Four cage models: (a): Type A cage; (b): Type B cage; (c): Type C cage; (d): Type D cage.

Ti6Al4V-SLM material properties used include a Young's modulus of 122,000 MPa, a Poisson's ratio of 0.3, a density of 4.4×10^{-3} g/mm^3, and a yield strength of 1062 MPa. Young's modulus and yield strength were obtained from tensile tests on self-manufactured Ti6Al4V samples, while Poisson's ratio and density were sourced from the literature.

In the Abaqus model setup, a uniformly elastic-plastic material with ductile and progressive damage evolution was used. The upper and lower rigid surfaces were defined as compression and support planes, respectively. All degrees of freedom were constrained on the support plane, while only the axial degree of freedom was allowed on the compression plane, restricting the remaining five degrees of freedom. To control variables, the stress distribution of the Tubular-G structure and the body-centered cubic (BCC) structure was observed under the same 1500 N load.

2.5. Design and SLM printing of cervical interbody cages

Combining the shape of commercially available cervical interbody cages and the placement of bone nails, we designed four interbody cage types. As shown in Fig. 6:

Regarding shape design, (a) is a 14 mm*11 mm*6 mm outer frame design with an inner opening window. (b) For 14 mm*12 mm*6 mm outer frame design with internal window opening. (c) For 14 mm*12 mm*6 mm outer frame design with no internal window opening. (d) For the 14 mm*12 mm*6 mm frame design with an internal window and an additional internal frame. For ease of presentation, (a) will be referred to as Type A, (b) as Type B, (c) as Type C, and (d) as Type D below. Type A has the same internal grid area design as Type B, but Type A has a narrower outer frame, Type C and Type D have the same outer frame design compared to Type B, but with a change in the design of the internal porous structural regions.

The cervical interbody cages were printed using the same machine and parameter settings as in 2.3. After printing, the samples were immersed in distilled water in an ultrasonic cleaner for half an hour to remove unsintered titanium alloy powder.

2.6. Mechanical testing of cervical interbody cages

Static/dynamic compression and subsidence experiments were performed according to ASTM-2077 to test the mechanical properties of the cage. As shown in Fig. 7.

For static compression, we recorded the displacement during compression and load and calculated the stiffness of the cage. The fusers were placed on the fixture of a universal testing machine (MTS-E44.305, USA) and axially compressed at a rate of 0.3 mm/min until the model was fractured, and the displacement load during compression was recorded. Each cage was tested three times and averaged to ensure the repeatability of the experiments.

The static settlement experiments were performed using the same universal testing machine as the static compression experiments, with the machine loaded at a rate of 0.3 mm/min. The load-displacement relationship was recorded, and the machine was loaded until the force-displacement curves displayed by the universal testing machine showed significant bending. The loads required to sink all the samples in a class 15 polyurethane foam test block were obtained.

2.7. Biocompatibility testing of cervical interbody cages

The cervical intervertebral cage was first tested for CCK-8 cytotoxicity. The experiment was divided into three groups: the control group (DMEM medium), the extract group, and the group where the medium was changed to extract when the cells were cultured with DMEM medium for 24 h. The number of cells was counted after 24 h, 48 h, 72 h, and 96 h of cell culture.

The cells used were mouse embryonic osteoblast precursor cells (MC3T3-E1). MC3T3-E1 cells were removed from the incubator and placed in a biological safety cabinet, the cell culture solution in the culture bottle was aspirated and discarded, 5 mL of PBS was

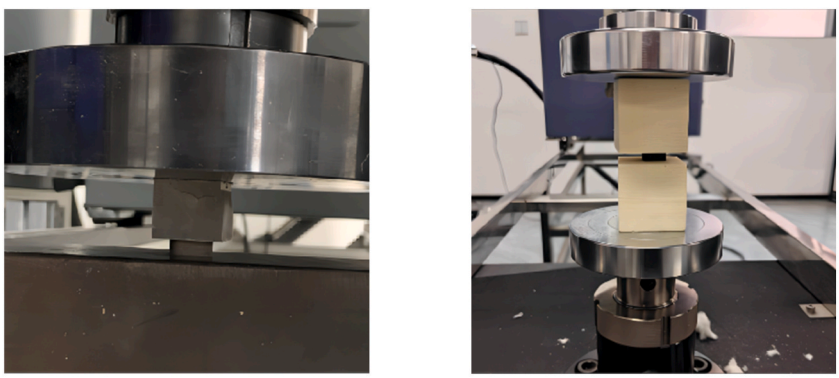

(**a**) (**b**)

Fig. 7. Mechanical testing of cervical interbody cage; (a): Static compression of cervical interbody cage; (b): Sinking experiment of cervical interbody cage.

added to the bottle to wash the cells to aspirate the PBS, 1 mL of trypsin digestion solution was added to the bottle, and the bottle was placed in an incubator to be digested for 3 min. After the digestion was completed, the cells were observed under the microscope to see whether they became ovoid or not, and 5 mL of complete culture medium was added to the bottle to Terminate the digestion; the cells repeatedly with a pipette, blow the cells into single cells, collect the cell suspension in a 15 mL centrifuge tube, centrifuge at 1000 RMP for 5 min; after centrifugation, discard the supernatant, and resuspend the cells by adding 1 mL of complete medium to the cell precipitate.

The extract was prepared with a 20-A cage apparatus according to ISO 10993 (37 °C, 24 h of extraction). The cell concentration was adjusted to 8×10^4/mL, and 100 μL of cell suspension was added to each well according to the experimental protocol. The cells were incubated in the incubator for 4 h to wait for cell attachment, and then the cells were attached to the wall. The culture medium of the extract group was discarded from the wells according to the protocol, and 100 μL of the extract was added to the wells to continue incubation. The culture medium of the group, replaced by the extract group, was changed to the extraction medium after 24 h. In contrast, the control group continued to use the complete culture medium.

According to the spiking table, 10 μL of CCK-8 reagent was added and incubated for 1 h at 24, 48, 72, and 96 h after cell attachment. After the incubation, the absorbance at 450 nm was measured by an enzyme marker, and the cell viability was calculated using the following formula.

$$\text{Cell viability } (\%) = [(\text{As-Ab}) \ / \ (\text{Ac-Ab})] \times 100\% \tag{2}$$

As: absorbance of the experimental group (with cells, medium, CCK-8 solution, and drug solution); Ac: absorbance of the control group (with cells, medium, CCK-8 solution, without drug); Ab: absorbance of the blank group (with medium, CCK-8 solution, without cells and drug).

After the completion of the extract experiments, MC3T3-E1 cells were seeded on the surface of each sample at a density of 8 × 104/mL, cultured for four days, and cell adhesion and proliferation were observed on the sample surface using electron microscopy.

3. Results

3.1. Research on compression properties of 3D printed Tubular-G structure

We investigated the mechanical properties of titanium alloy samples with Tubular-G structures at different volume fractions. Using Ashby's theory, we developed mathematical formulas to relate the equivalent modulus of elasticity, yield strength, and porosity. Young's modulus, yield stress, and maximum stress were calculated from the force-displacement data obtained during compression testing. The results are presented in Table 2.

The compression image of a Tubular-G structure with a 50 % volume fraction (Fig. 8) is used as an example to demonstrate the compression process. The image shows the same trend as other studies [29]: (i) firstly, an elastic loading phase, and (ii) as it continues to be compressed, it crosses the yield strength and then enters into the plastic phase. Eventually the structure suffered a brittle fracture and compression stopped.

According to Ashby's theory, the equivalent modulus of elasticity and yield stress of a porous structure can be expressed as a function of volume fraction, Eq:

$$\mathbf{E}^* = \mathbf{E_s} \bullet \mathbf{C_E} \cdot \left(\frac{\rho^*}{\rho_s}\right)^{\mathbf{m_E}} \tag{2a}$$

$$\sigma^* = \sigma_s \bullet \mathbf{C}_\sigma \cdot \left(\frac{\rho^*}{\rho_s}\right)^{\mathbf{m}_\sigma} \tag{3}$$

Among them. E^*, σ^*, and ρ^* are the equivalent modulus of elasticity, yield strength, and density of the porous structure, and the E_S, σ_S, and ρ_S are Young's modulus, yield strength, and density of the material (Ti6Al4V in this paper), C_E and C_σ are constants and ρ^* / ρ_S is relative density from the static compression results of the Tubular-G structure in Table 3 and Eq. (2)(3), We fitted the equations and images of the equivalent modulus of elasticity and yield stress concerning the relative density shown in Fig. 9.

3.2. Stress distribution in Tubular-G structures

To intuitively and concisely assess whether stress concentration occurs in the Tubular-G structure, we extracted the stress contour plots for four different volume fractions of the Tubular-G structure and the body-centered cubic structure under a static compression load of 1500 N. This comparison highlights the advantages and disadvantages of each structure.

Table 2
Yield strength, maximum stress, and Young's modulus of Tubular-G.

	20 % volume fraction	30 % volume fraction	50 % volume fraction	70 % volume fraction
Yield stress (MPa)	58.57 ± 0.24	121.62 ± 1.10	268.51 ± 10.92	536.43 ± 8.53
Maximum stress (MPa)	62.40 ± 0.74	128.5 ± 0.72	305.9 ± 2.29	618.33 ± 2.56
Young's modulus (MPa)	867.33 ± 6.03	2121.5 ± 111.02	3377.2 ± 14.03	5488.17 ± 286.18

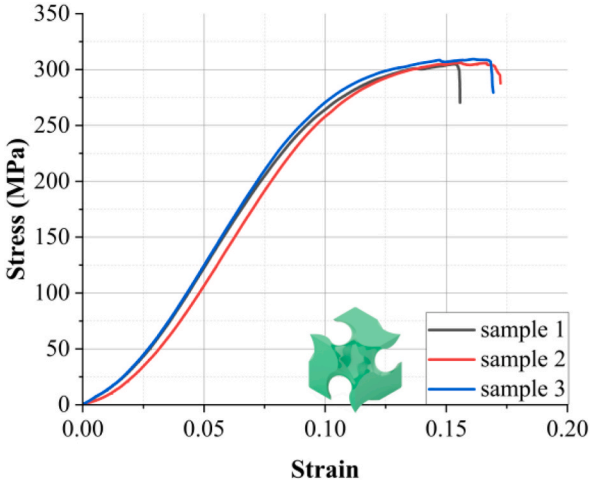

Fig. 8. Compressed image of Tubular-G structure at 50 % volume fraction.

Table 3
Relative cell proliferation rate of the three groups after 24 h, 48 h, 72 h, 96 h.

groups	24 h	48 h	72 h	96 h
Control subjects	100 ± 3.604	100 ± 3.658	100 ± 8.931	100 ± 7.283
Extracts	92.197 ± 10.963	98.262 ± 7.77	100.561 ± 5.307	96.731 ± 7.072
Replacement of the leachate group after 24 h	103.094 ± 11.43	101.204 ± 5.24	94.34 ± 4.766	99.353 ± 5.72

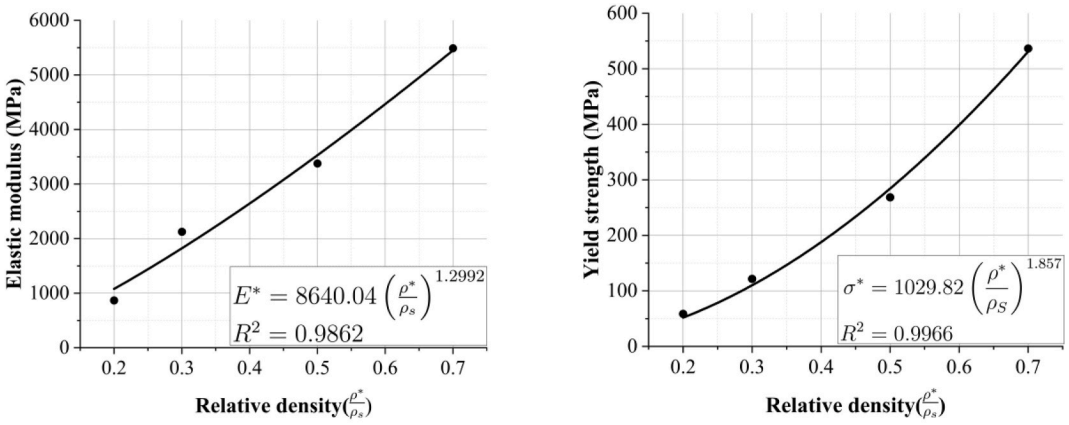

Fig. 9. Image of equivalent modulus of elasticity and yield stress with respect to relative density; (a): Ashby's formula for relative density versus Young's modulus; (b): Ashby's formula for relative density versus yield strength.

The stress contour plots for the Tubular-G structures with four different volume fractions and the body-centered cubic structure under a 1500 N load are shown in Fig. 10. In the 20 % and 30 % volume fraction Tubular-G structures, as well as the body-centered cubic structure, some nodes exhibit stress values exceeding the material's maximum yield strength. This occurs because Abaqus calculates stress at integration points and then distributes it to the nodes, which can result in node stresses that surpass the material's maximum yield strength.

Under the 1500 N load, the strains for the Tubular-G structures are as follows: 0.7 % for the 20 % volume fraction, 0.25 % for the 30 % volume fraction, 0.06 % for the 50 % volume fraction, and 0.02 % for the 70 % volume fraction. In contrast, the strain for the body-centered cubic structure is 1.11 %.

The stress distribution in the four Tubular-G structures is relatively uniform along the axial direction of the compression load. In contrast, the stress in the body-centered cubic structure is mainly concentrated at the connecting points, as shown in Fig. 10, where these points exhibit much higher stress levels than the surrounding areas. The internal stress distribution within the Tubular-G

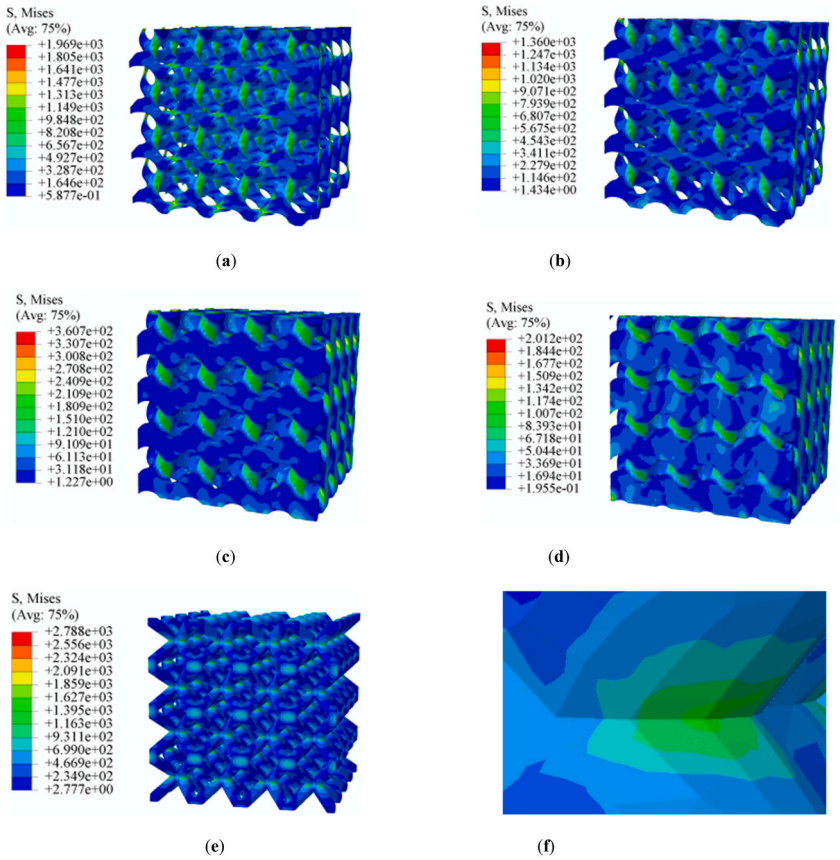

Fig. 10. Stress contour plots of the five models under peak load. (a) Tubular-G structure with 20 % volume fraction; (b) Tubular-G structure with 30 % volume fraction; (c) Tubular-G structure with 50 % volume fraction; (d) Tubular-G structure with 70 % volume fraction; (e) Body-centered cubic structure; (f) Connecting points of the Body-centered cubic structure.

structures is more even, with no signs of stress concentration, demonstrating superior mechanical performance.

3.3. Axial compression and subsidence experiments with cervical interbody cages

Based on the results from sections 3.1 and 3.2, the Tubular-G structures with lower Young's modulus and yield strength, and the more suitable pore sizes, were selected for the fabrication of cervical interbody cages. Specifically, the Tubular-G structures with 20 % and 30 % volume fractions were chosen. Eight cervical interbody cages were designed using these Tubular-G structures in combination with the four types of cages described in section 2.5. The printing of these cages was completed, as shown in Fig. 11.

In the following, the cervical interbody cages with 20 % volume fraction Tubular-G structures are called Type 20-A, 20-B, 20-C, and 20-D (see Fig. 12). The cervical interbody cages with 30 % volume fraction Tubular-G structures are Type 30-A, 30-B, 30-C, and 30-D. The stiffness of the cervical interbody cages was determined by dividing the loads obtained by each cage by the displacement of the

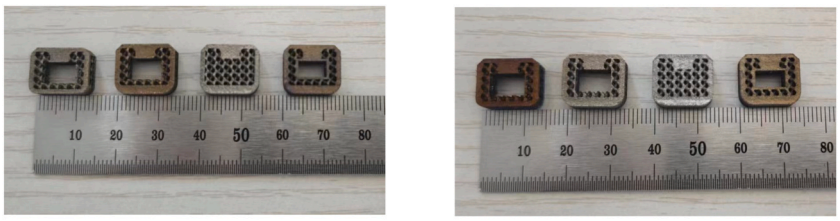

Fig. 11. Titanium interbody cage made by 3D printing; (a): Cervical interbody cage with 20 % volume fraction Tubular-G structure, from left to right, Types A, B, C, D of the design in 2.5, respectively; (b): Cervical interbody cage with 30 % volume fraction Tubular-G structure, from left to right, Types A, B, C, D of the design in 2.5, respectively.

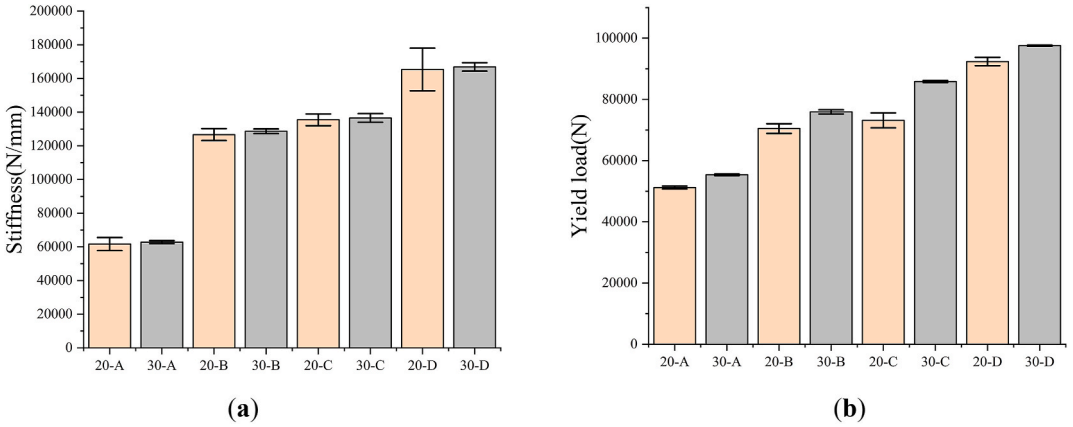

Fig. 12. Stiffness and yield load of the cervical interbody cage; (a): Stiffness; (b): Yield Load.

cages to obtain the stiffness.

Axial compression experiments were performed on the eight cervical interbody cages mentioned above, with three samples of each cage, and the resulting loads were divided by the displacements to derive the stiffness of the cervical interbody cage. Type A and Type B are used to compare the effects of different outer frame designs on the cages. Types B, C, and D are employed to assess the impact of varying porous structural designs on the cages. It is observed that Type B exhibits significantly higher stiffness and yield strength compared to Type A. This indicates that the outer frame design has a more substantial effect on stiffness and yield load. In contrast, the differences in stiffness and yield strength from Type B to Type D are relatively minor, suggesting that the impact of the internal porous structure on these properties is less pronounced. The stiffness and yield strength of the same type of cage with a 30 % volume fraction porous structure is greater than that of the cage with a 20 % volume fraction porous structure. When considered collectively, the stiffness is the least for the 20-A cage and the 30-A cage. The difference in stiffness between the cages and cones is too significant to cause the cages to settle; in order to minimize the settlement, we chose these 20-A and 30-A cages for the settlement experiments and biocompatibility testing. Their static compression curves are shown in Fig. 13.

The 20-A and 30-A cages were selected for the subsidence experiment, during which the cervical interbody cage samples were plunged into the polyurethane block without deformation, and the test data were fitted by Origin software to obtain the load-displacement curves of the two types of cervical interbody cages and the polyurethane block as shown in Fig. 14. The curves showed that the test curves of the two types of cages showed the same trend. The reason is that the stiffness of the polyurethane material is much smaller than that of the titanium alloy, and the load is much higher than the yield limit of the polyurethane block during the compression process, so the cage is plunged into the phenomenon of the polyurethane block.

The stiffness of the polyurethane block, $\mathbf{k_2}$, can be used to reflect the degree to which the cage sinks into the vertebral body, with smaller values of $\mathbf{k_2}$ indicating a greater distance for the cervical interbody cage to sink into the vertebral body. After the axial compression subsidence test, the stiffness $\mathbf{k_0}$ of the polyurethane block and cervical interbody cage system was calculated, and the cervical interbody cage stiffness $\mathbf{k_1}$ was derived from the static compression test. The following relational equation was satisfied between these three:

$$\mathbf{k_2} = \frac{\mathbf{k_0 k_1}}{\mathbf{k_1} - \mathbf{k_0}} \tag{4}$$

Where k_0 is the stiffness of the polyurethane block and cage system, k_1 is the cervical interbody cage stiffness, and k_2 is the polyurethane block stiffness.

After calculation, the polyurethane block stiffness of the 20-A cage was 348.33 N/mm, and the polyurethane block stiffness of the 30-A cage was 319.07 N/mm. The sinking performance of the 20-A cage is slightly higher than the sinking performance of the 30-A cage.

3.4. Biocompatibility testing of cervical interbody cages

The safety of the cage material was verified by the CCK-8 in vitro cytotoxicity assay, in which mouse embryonic osteoblast precursor cells were cultured in the medium of three groups and then tested with CCK-8 reagent. The relative cell proliferation rate was calculated. The results are shown in Table 3.

According to ISO 10993-5-2009 Biological Standard for Medical Devices, in vitro cytotoxicity test [30], the relative cell proliferation rate of the specimen was more significant than 70 %, which can be considered non-toxic. The cervical interbody cage materials are non-toxic and can be implanted back into the animal, which is good biosafety.

As shown in Fig. 15, after four days of incubation, some cells started to attach to the surface of the cage. 30-A cage had significantly more attached cells than a 20-A cage, which might be related to the pore size of both devices. 30-A cage had a pore size of 1200 μm for

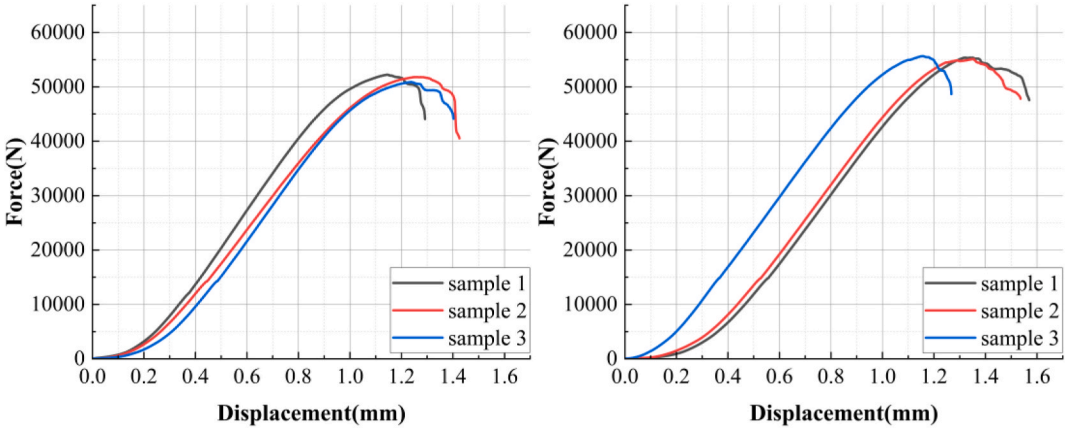

Fig. 13. Compression curves of the cervical interbody cage; (a): 20-A; (b):30-A.

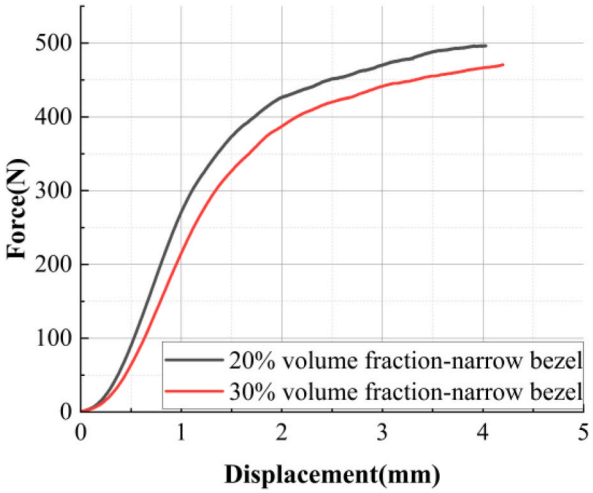

Fig. 14. Load-displacement curves of the two types of cervical interbody cages and the polyurethane block.

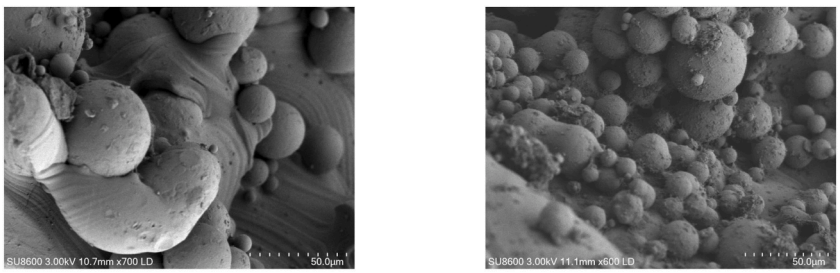

(**a**) (**b**)

Fig. 15. Cell attachment to the cage; (a) 20-A cage; (b) 30-A cage.

the 30 % volume fraction of the Tubular-G structure, which was smaller than the pore size (1460 μm) of the 20 % volume fraction of the Tubular-G structure for the 20-A cage. Structure's pore size (1460 μm). The results showed that the 30-A cage apparatus had better cell attachment ability.

4. Discussion

This paper investigated a cervical interbody cage designed based on TPMS principles, utilizing a Tubular-G porous structure fabricated through 3D printing technology to leverage the benefits of TPMS. The study focused on evaluating two key metrics of the cervical interbody cage: mechanical properties and biocompatibility, to ensure its safety and stability within the human body. The findings are expected to offer a new, practical approach for improving cage performance and minimizing postoperative complications.

Cage design requires a balance between mechanical properties and a porous structure that accommodates cell growth. The smooth pore structure of the Tubular-G design allows the Young's modulus of the structure to be adjusted to match that of human bone while providing space for cell growth. This paper investigated the relationship between the Tubular-G structure and its mechanical properties to determine Young's modulus and yield strength at different porosities. The results indicate that Young's modulus and yield strength of the Tubular-G structure increase with porosity, displaying mechanical properties comparable to other porous materials [13,14]. For a single cell size of 2 mm, the Young's modulus and yield strength of the Tubular-G structure at a 20 % volume fraction were 867.33 MPa and 58.57 MPa, respectively. At a 30 % volume fraction, these values were 2125 MPa and 121.62 MPa, respectively. The Young's modulus of these structures falls between that of cortical and cancellous bone, while the yield strengths are higher than those of cancellous bone. Human cancellous bone has a Young's modulus of 20 MPa–640 MPa and an ultimate strength of 0.9 MPa–8.8 MPa, while cortical bone has a Young's modulus of 13,600 MPa-23,830 MPa and a yield strength of 80–156 MPa. This range helps reduce the effect of "stress shielding" on human bones, suggesting that Tubular-G has significant potential as a cage design structure.

Stress concentration in fusion devices can lead to structural failure. Therefore, we conducted a finite element analysis to compare the internal stress distribution of the Tubular-G structure with that of the body-centered cubic structure. The results revealed that the Tubular-G structure exhibited a relatively uniform stress distribution with no significant signs of stress concentration. This uniformity is attributed to the advantages of the highly twisted and topologically complex porous structure provided by the TPMS design. In contrast, stress concentrations are often observed at the connection points in porous structures based on strut designs [31]. We observed significantly higher stress at these connecting points in the body-centered cubic structure, which could reduce the implant's lifespan.

Based on the Tubular-G structure, eight different shapes and sizes of cervical interbody cages were designed and tested for their static compression performance in this study. We separately explored the effects of the outer frame design and the porous structure region on the overall performance of the cages. To address the issue of "stress shielding," we selected the 20-A and 30-A cages, which had the lowest stiffness, for subsidence experiments. The results showed that the sinking performance of the two cages was similar, with the 20-A cage exhibiting slightly better performance than the 30-A cage.

In addition to the mechanical properties, the cage's biocompatibility also affects the implant's safety in the human body. In this paper, the biocompatibility test of the cage was carried out, and the results of the CCK-8 cytotoxicity test showed that the cage material was non-cytotoxic and had good biological safety. This provides a vital safety guarantee for the clinical application of Tubular-G structural cages. The cell adhesion test showed that both cages had cell adhesion. However, the cell adhesion of the 30-A cage was significantly more than that of the 20-A cage, and the two cages showed a significant difference in cell adhesion ability. The combined mechanical properties and biocompatibility tests showed that the 30-A cage was more compatible with the cervical interbody cage.

However, this study has several areas for improvement. Firstly, the mechanical property tests were limited in scope, and a more comprehensive set of tests could enhance the reliability of the results. Future studies should include additional tests to provide a more thorough evaluation. Additionally, the current cage design is relatively basic, featuring only two types of outer frames and three types of porous structural regions. This limited variety may not be universally applicable. Future work should explore more diverse designs for both the outer frames and porous structures, using stiffness and subsidence performance as key variables to develop more robust conclusions.

In summary, cervical interbody cages designed based on TPMS exhibit excellent mechanical properties and good biocompatibility, making them promising candidates for cervical spine surgery. Nevertheless, further optimization of design, in vivo experiments, and comparisons with other types of cages are necessary to provide comprehensive evidence for their clinical application.

5. Conclusions

In the study of interbody cages, most research tends to focus on the overall design of the fusion device, while detailed investigations into the internal porous structure of the interbody cage are less common. The exceptional mechanical properties and unique characteristics of TPMS structures have been extensively documented. In this study, we explored the Tubular-G structure derived from TPMS and demonstrated its effectiveness in adjusting Young's modulus, yield strength, and stress distribution to mitigate the issue of stress concentration. The Tubular-G structures with 20 % and 30 % volume fractions showed mechanical properties comparable to human bone. Specifically, the 3D-printed TC4-based porous cervical interbody cages featuring Tubular-G structures exhibited low stiffness, high compressive strength, and good biocompatibility, positioning them as promising candidates for treating cervical disc injuries. Moving forward, we plan to further optimize both the fusion rim and the porous structural region to enhance cage design and performance.

Funding

This research was funded by Research and Application of Key Technologies for Advanced Wearable Health Equipment (2202305B008), Development of Customized 3D Printed TC4-Based Graded Porous Spinal Interbody Fusion Devices (202304B046),

Research and Development of 3D Printed Hydrogel-Based Skin Sensors (KY202403), Bio-3D Printed In Situ Mineralized Bone Tissue Engineering Scaffold (KY202406), and Chengde Biomedicine Industry Research Institute Funding Project (202205B086).

Data availability statement

Not applicable. The authors do not have permission to share data.

CRediT authorship contribution statement

Kun Li: Writing – original draft, Software, Resources, Project administration, Methodology, Conceptualization. **ChunYan Tian:** Project administration, Methodology. **QiuJiang Wei:** Supervision, Formal analysis. **XinRui Gou:** Project administration, Methodology, Investigation. **FuHuan Chu:** Visualization, Supervision. **MengJie Xu:** Formal analysis. **LinHui Qiang:** Writing – review & editing, Visualization, Resources, Formal analysis, Data curation, Conceptualization. **ShiQi Xu:** Writing – review & editing, Visualization, Funding acquisition, Formal analysis.

Declaration of competing interest

The authors declare no conflict of interest.

References

[1] W.M. Tavares, S.A. de França, W.S. Paiva, et al., A systematic review and meta-analysis of fusion rate enhancements and bone graft options for spine surgery, Sci. Rep. 12 (1) (2022) 7546.
[2] B.D. Elder, W. Ishida, C.R. Goodwin, et al., Bone graft options for spinal fusion following resection of spinal column tumors: systematic review and meta-analysis, Neurosurg. Focus 42 (1) (2017) E16.
[3] M. Antoni, Y.P. Charles, A. Walter, et al., Fusion rates of different anterior grafts in thoracolumbar fractures, J. Spinal Disord. Tech. 28 (9) (2015) E528–E533.
[4] C.T. Pan, C.H. Lin, Y.K. Huang, et al., Design of customize interbody fusion cages of Ti64ELI with gradient porosity by selective laser melting process, Micromachines 12 (3) (2021) 307.
[5] J.H. Tan, C.K. Cheong, H.W.D. Hey, Titanium (Ti) cages may be superior to polyetheretherketone (PEEK) cages in lumbar interbody fusion: a systematic review and meta-analysis of clinical and radiological outcomes of spinal interbody fusions using Ti versus PEEK cages, Eur. Spine J. 30 (2021) 1285–1295.
[6] N.A. Patel, S. O'Bryant, C.D. Rogers, et al., Three-dimensional-printed titanium versus polyetheretherketone cages for lumbar interbody fusion: a systematic review of comparative in vitro, animal, and human studies, Neurospine 20 (2) (2023) 451.
[7] Y. Li, C. Yang, H. Zhao, et al., New developments of Ti-based alloys for biomedical applications, Materials 7 (3) (2014) 1709–1800.
[8] L. Wang, B. Yuan, F. Chen, et al., The ability of a novel biomimetic titanium alloy cage in avoiding subsidence and promoting fusion: a goat spine model study, Mater. Des. 213 (2022) 110361.
[9] M. Cronskär, M. Bäckström, L.E. Rännar, Production of customized hip stem prostheses–a comparison between conventional machining and electron beam melting (EBM), Rapid Prototyp. J. 19 (5) (2013) 365–372.
[10] C. Yee-Yanagishita, G. Fogel, B. Douglas, et al., Biomechanical comparison of subsidence performance among three modern porous lateral cage designs[J], Clin. BioMech. 99 (2022) 105764.
[11] C.H. Li, C.H. Wu, C.L. Lin, Design of a patient-specific mandible reconstruction implant with dental prosthesis for metal 3D printing using integrated weighted topology optimization and finite element analysis, J. Mech. Behav. Biomed. Mater. 105 (2020) 103700.
[12] K.K. Alaneme, S.A. Kareem, B.N. Ozah, et al., Application of finite element analysis for optimizing selection and design of Ti-based bimetallic alloys for fractures and tissues rehabilitation: a review, J. Mater. Res. Technol. 19 (2022) 121–139.
[13] E. Alabort, D. Barba, R.C. Reed, Design of metallic bone by additive manufacturing, Scripta Mater. 164 (2019) 110–114.
[14] D. Barba, E. Alabort, R.C. Reed, Synthetic bone: design by additive manufacturing, Acta Biomater. 97 (2019) 637–656.
[15] L.Y. Zhu, L. Li, Z.A. Li, et al., Design and biomechanical characteristics of porous meniscal implant structures using triply periodic minimal surfaces, J. Transl. Med. 17 (1) (2019) 1–10.
[16] B. Liu, J. Feng, Z. Lin, et al., Controllable three-dimension auxetic structure design strategies based on triply periodic minimal surfaces and the application in hip implant, Virtual Phys. Prototyp. 18 (1) (2023) e2170890.
[17] N. Novak, O. Al-Ketan, L. Krstulović-Opara, et al., Quasi-static and dynamic compressive behaviour of sheet TPMS cellular structures, Compos. Struct. 266 (2021) 113801.
[18] M. Zhao, X. Li, D.Z. Zhang, et al., TPMS-based interpenetrating lattice structures: design, mechanical properties and multiscale optimization, Int. J. Mech. Sci. 244 (2023) 108092.
[19] P. Shang, B. Ma, G. Hou, et al., A novel artificial vertebral implant with Gyroid porous structures for reducing the subsidence and mechanical failure rate after vertebral body replacement, J. Orthop. Surg. Res. 18 (1) (2023) 828.
[20] A.H. Schoen, Infinite Periodic Minimal Surfaces without self-intersections[R], 1970.
[21] V. Saranathan, S. Narayanan, A. Sandy, et al., Evolution of single gyroid photonic crystals in bird feathers[J], Proc. Natl. Acad. Sci. USA 118 (23) (2021) e2101357118.
[22] V. Saranathan, C.O. Osuji, S.G.J. Mochrie, et al., Structure, function, and self-assembly of single network gyroid (I 4132) photonic crystals in butterfly wing scales, Proc. Natl. Acad. Sci. USA 107 (26) (2010) 11676–11681.
[23] X. Du, S. Ronayne, S.S. Lee, et al., 3D-printed PEEK/silicon nitride scaffolds with a triply periodic minimal surface structure for spinal fusion implants, ACS Appl. Bio Mater. 6 (8) (2023) 3319–3329.
[24] M. Zhao, D.Z. Zhang, F. Liu, et al., Mechanical and energy absorption characteristics of additively manufactured functionally graded sheet lattice structures with minimal surfaces, International Journal of Mechanical Sciences 167 (2020) 105262.
[25] Hui Yang, Research on Modeling Method of Porous Structure [D], Southeast University, Nanjing, 2017, p. 21 (In Chinese).
[26] V. Karageorgiou, D. Kaplan, Porosity of 3D biomaterial scaffolds and osteogenesis, Biomaterials 26 (27) (2005) 5474–5491.
[27] S.J. Hollister, C.Y. Lin, E. Saito, et al., Engineering craniofacial scaffolds, Orthod. Craniofac. Res. 8 (3) (2010) 162–173.
[28] I. Maskery, A.O. Aremu, L. Parry, et al., Effective design and simulation of surface-based lattice structures featuring volume fraction and cell type grading, Mater. Des. 155 (2018) 220–232.

[29] F.S.L. Bobbert, K. Lietaert, A.A. Eftekhari, et al., Additively manufactured metallic porous biomaterials based on minimal surfaces: a unique combination of topological, mechanical, and mass transport properties, Acta Biomater. 53 (2017) 572–584.
[30] I. Iso, 10993–5: 2009 Biological Evaluation of Medical Devices—Part 5: Tests for in Vitro Cytotoxicity, International Organization for Standardization, Geneva, 2009, p. 34.
[31] M.T. Hsieh, M.R. Begley, L. Valdevit, Architected implant designs for long bones: advantages of minimal surface-based topologies, Mater. Des. 207 (2021) 109838.